Explicit electrification and lightning forecast implemented within the WRF-ARW model.

Alexandre O. Fierro[1], Edward R. Mansell[2], Conrad L. Ziegler[2] and Donald R. MacGorman[2]
[1]Cooperative Institute for Mesoscale Meteorological Studies, Norman, Oklahoma, USA.
email: afierro@ou.edu
[2]National Severe Storms Laboratory/NOAA/OAR, Norman, Oklahoma USA,

ABSTRACT: Lightning threats in present-day numerical weather prediction models are currently diagnosed from model variables such as graupel mixing ratio and ice water content that are known to be well correlated with the occurrence of lightning. To provide a more physically sound assessment of lightning threat, an explicit charging/discharge model (with explicit elliptic solution of the 3D component of the ambient electric field) has been successfully implemented into the NSSL two-moment microphysics scheme within the WRF-ARW model (Fierro et al. 2013). Results from convection-allowing (3-km) benchmark simulations of a major hurricanes, a winter storm and a severe continental mesoscale convective system will be presented and evaluated against total lightning data observations from the EarthNetworks® and the Los Alamos Sferic Array (LASA).

Recently, the discharge physics of this lightning model have been upgraded from a bulk code to a well-documented hybrid three-dimensional scheme, allowing to resolve and forecast flash type and polarity. Results from benchmark cloud-resolving (500-m) simulation of Hurricane Isaac (2012) will be briefly reviewed.

INTRODUCTION AND BRIEF DESCRIPTION OF THE LIGHTNING MODEL

Lightning in present day numerical weather prediction models (NWP) is either explicitly predicted using electrification physics or diagnosed via combinations of kinematic and/or microphysical proxy variables known to be well correlated with the occurrence of lightning (e.g., graupel volume, ice water path; McCaul et al. 2009).

In the last three decades, several studies successfully implemented lightning parameterization schemes and electrification physics within cloud-resolving numerical models (e.g., Rawlins 1982; Takahashi 1984; Helsdon and Farley 1987; Ziegler et al. 1991; Mansell et al. 2005).

The present WRF explicit lightning module (Fierro et al. 2013) includes in-cloud non-inductive and inductive collisional charging, explicit calculation of the ambient vector electric field, and two discharge parameterizations (one bulk and one three dimensional). For brevity, this section presents parameterization equations only for the charging mechanisms (inductive and non-inductive charge exchange) and lightning. The reader is invited to consult Fierro et al. (2013) for a complete description of this lightning model.

A series of classic laboratory studies have suggested that a mechanism involving rebounding collisions between ice crystals and riming graupel pellets is the primary *in situ* charging mechanism within thunderstorms (e.g., Takahashi 1978; Saunders and Peck 1998; Takahashi and Miyawaki 2002; Emersic and Saunders 2010). When cloud-scale simulations assumed a typical population of mixed-phase particles within a convective cloud in nature, the integrated effect of the charge separated per collision via this process was able to generate electric fields comparable in magnitude to those observed in thunderstorms (e.g., Takahashi 1984; Helsdon et al. 2001; Mansell et al. 2005; Fierro et al. 2006, 2008).

Noninductive charge separation during a rebounding collision between graupel–hail and snow–cloud ice is parameterized in our new module following Eq. (7) of Mansell et al. (2005):

$$\partial\rho_{xy} / \partial t = \beta\delta q_{xy}(1 - E_{xy})E_{xy}^{-1}n_{xacy},$$

where ρ_{xy} is the space charge (C m^{-3}) separated during a collision between hydrometeor species x and y, δq_{xy} is the weighted average separated charge (C) per rebounding collision between hydrometeor species x and y, ß is an arbitrary factor limiting charging at low temperatures (owing to a lack of experimental data), n_{xacy} is the number concentration collection rate integral, and E_{xy} is the collection efficiency. In this parameterization, the magnitude of charge separated within a grid cell (δq) is calculated from a polynomial fit of the noninductive critical charging curve as a function of temperature and graupel–hail riming accretion rate, given by Eq. (18) of Mansell et al. (2005):

$$\delta q = BD_I^a(V_g - V_I)^b q(RAR),$$

where B, a, and b are a function of crystal size (Table 1 in Mansell et al.); D_I is the mean volume diameter of the ice crystal–snow, V_g and V_I are the mass-weighted mean terminal fall speeds for graupel and cloud ice (or snow), respectively; and $q(RAR)$ is the charge separation as a function of the riming accretion rate (RAR) from Brooks et al. (1997), modified by Mansell et al. (2005).

Inductive charging becomes significant in regions of relatively strong electric fields. The inductive charging rate incorporated in our module follows Ziegler et al. (1991). Because of the low conductivity of ice and comparatively short contact time during collision, inductive charge separation during ice–ice collisions was assumed negligible. Therefore, only collisions between cloud water and ice–graupel–hail are considered following Eq. (27) of Mansell et al. (2005):

$$\partial\rho_g/\partial t = (\pi^3/8)[6.0V_g/\Gamma(4.5)]\, E_{gc}E_r\, n_{t,c}n_{0,g}D_c^2\, [\pi\Gamma(3.5)\varepsilon\langle\cos\theta\rangle E_z\Delta_{n,g}^2 - \Gamma(1.5)\rho_g/(3n_{t,g})],$$

where ρ_g is the charge density carried by graupel; D_c is the cloud droplet diameter; E_{gc} is the collision efficiency between graupel and cloud water; E_r is the rebound probability; $n_{t,c}$ and $n_{t,g}$ are the total cloud water and graupel number densities, respectively; V_g is the mass-weighted mean fall speed of graupel; $\Gamma(x)$ is the complete gamma function; $\Delta_{n,g}$ is the characteristic diameter of graupel; $n_{0,g}$ is the number concentration intercept for graupel; $\langle\cos\theta\rangle$ is the average cosine of the angle of rebounding collision; E_z is the vertical component of the electric field; and ε is the electrical permittivity of air.

The amount of positive charge gained by one type of hydrometeor in a grid box due to a given process is balanced by an equal amount of negative charge gained by the interacting hydrometeor. At each time step, the total charge gained by each hydrometeor type in a grid cell via inductive and non inductive charging, mass exchange, sedimentation and advection is determined. Subsequent wind shear/advection and differential sedimentation of particles having different terminal fall speeds can separate positive and negative charge, and the charge on precipitation is allowed to pass through the lower boundary, thus leaving the domain.

The electric field from the resulting charge distribution is computed explicitly by solving the Poisson equation for the scalar electric potential using a computationally efficient “Black Box” multigrid solver (BOXMG, Dendy 1987; 2010). From this solution, the vector electric field are then calculated from the negative gradient of the potential.

When the magnitude of the electric field at any grid point exceeds the breakdown value indicated by Gurevich et al. (1992), lightning occurs by a crude but computationally efficient bulk discharge process adapted from Ziegler and MacGorman (1994, hereafter ZM94). The intent of this method is not to estimate flash rates or flash polarity realistically, as done by more sophisticated techniques (e.g., MacGorman et al. 2001, Mansell et al. 2002), but to identify storms that will produce lightning and to provide a rough, first-order indication of the expected relative amount of lightning at minimal computational cost. (Benchmark simulations revealed that the computational cost is roughly 10% over

control runs without explicit electrification and lightning.)

A discharge in the ZM94 approach is centered around each initiation point and involves all points within a fixed radius R (typically twice the horizontal grid spacing or 2-10 km), extending vertically through the entire depth of the simulation domain. To determine the charge involved in a flash, the magnitude of positive charge and the magnitude of negative charge are summed separately from all gridpoints with net charge exceeding a small threshold of charge magnitude (typically 0.1 nC m^{-3}) within the cylinder. The magnitude of each charge polarity effectively neutralized by a flash is a fraction (30%) of the maximum of these two sums. This is effected at each grid point by adding an amount of opposite charge polarity equal to 30% of the grid point's excess charge, adjusted so that the total positive charge involved in the flash equals the total negative charge in the flash. The charge is distributed among hydrometeor species in the grid box in proportion to the relative surface area of each species. The discharge procedure is repeated iteratively during a computational time step until the maximum electric field in the entire model domain no longer exceeds the threshold for flash initiation.

RESULTS

A preliminary real case benchmark simulation for Hurricane Rita at 3-km grid spacing (Fierro et al. 2013, their Fig. 11) using the 2-D bulk discharge code from ZM94 revealed the ability of this simplistic scheme to reproduce (i) the observed eyewall gross charge structure of this hurricane (i.e., normal tripole, Fierro et al. 2007; Fierro and Reisner 2011) and (ii) the overall simulated flash pattern consistent with the LASA observations (Shao et al. 2006; Fierro et al. 2011).

Aside from hurricanes, the WRF lightning model with the ZM94 scheme has been tested in a wide variety of convective regimes against total lightning data obtained from ENTLN (Fierro et al. 2013). Such convective regimes include severe continental convection (Fig. 1), winter storms, and tropical sea-breeze thunderstorms (not shown). Given a reasonable reproduction of the observed storms, the simulated spatial pattern of 1-h accumulated flash origin density (FOD) shows overall good agreement with the total lightning observations from ENTLN (Fierro et al. 2013, Fig. 1).

Vertical cross sections of key microphysical and electric variables through a mature convective cell in the quasi-linear MCS help provide a more detailed insight on the modeled lightning production process via ZM94 (Fig. 2). The updrafts and graupel mixing ratio in this intense leading-line cell exceed 10 m s^{-1} and 4 g kg^{-1} (Fig. 2a) respectively with 30 dBZ echo tops reaching an altitude of 12 km (Fig. 2a). From the Saunders and Peck (1998) charging curve, graupel charges positively within regions of relatively strong updrafts and larger LWC ($\geq$0.5 g m^{-3}) such as at (-99.1°W) and 5 km AGL (Fig. 2a, c). Conversely, graupel charges negatively in relatively lower LWC at (-99.2°W) and 7 km AGL (Fig. 2a, c). Inductive charging rates (ICR) in this convective cell are overall one order of magnitude smaller than non-inductive charging rates (NICR) and are primarily positive (Fig. 2c). The spatial sign-magnitude distribution of NICR and ICR accounts for the presence of distinctive pockets of strong magnitude

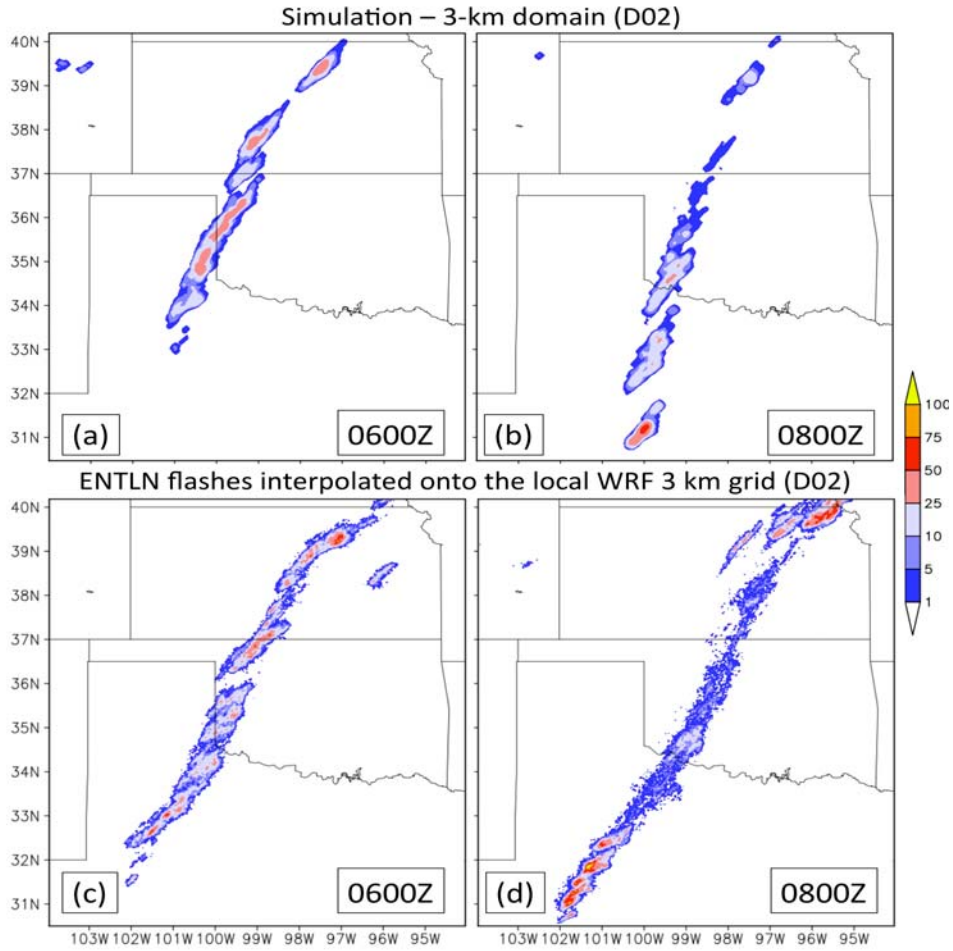

Figure 1. Simulated flash origin density (FOD, per grid cell h^{-1}) with ZM94 shown in (a) and (b) and the ENTLN total lightning data interpolated onto the local 3-km domain (D02) shown in (c) and (d). The FOD were summed for an hour prior to the times shown in the figures. Legends for colors and shadings are shown on the right of the figure. Figure adapted from Fierro et al. (2013).

(>100 pC m^{-3}) net negative and positive space charge below the -20°C level (Fig. 2d). Other charge pockets such as seen at (-99.6°W) above 8 km are likely due to advection and/or are leftover charge from a decaying cell in the trailing stratiform zone of the MCS (between -99.4° and -99.6°W) as evidenced for example by the weak vertical velocities (< 5 m s^{-1}) and small graupel mixing ratios (<1.5 g kg^{-1}) in this region (Fig. 2a). The simulated charge structure in this convective cell is generally complex and composed of several charge layers. The simulated vertical arrangement of net charge cannot be classified as simple dipoles nor tripoles (Wiliams, 1989) and, therefore, would be more consistent with the conceptual model of Stolzenburg et al. (1998) for continental MCS. Regions of relatively large electric field magnitude (E_{mag}) exceeding 75 kV m^{-1} are generally found between opposite-sign space charge centers such as at (99°W-98.4°W, z=8-12 km AGL, Fig. 2b, d) and (99.7°W-99.5°W, z=8-11 km AGL, Fig. 2b, d). Because the cross sections in Fig. 2 are shown after the discharge, smaller E_{mag} values are generally over and around updraft core regions (e.g., 99.4°W-99.1°W, z=5-12 km AGL, Fig. 2b).

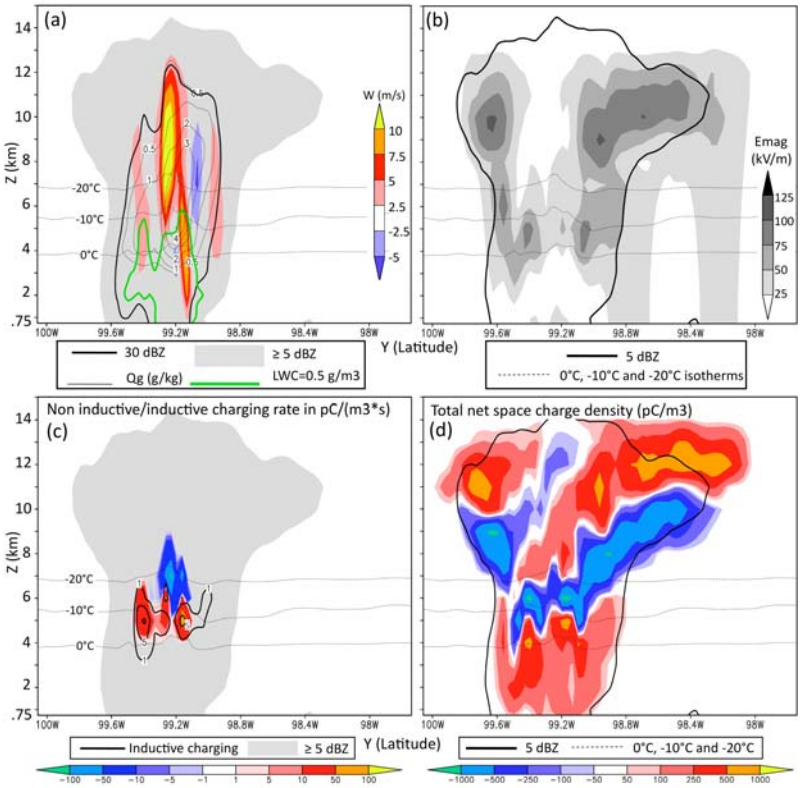

Figure 2. Vertical cross sections in the *XZ* plane through the convective cell shown in Figure 3a (0600) of main simulated electrical and microphysical variables with (a) showing vertical velocities (m s^{-1}, shading), 30 dBZ echo top (thick black contour), 0.5 g m^{-3} liquid water content (LWC, green contour) and graupel mixing ratio contours in 1 g kg^{-1} increments with the 0.5 g kg^{-1} contour also shown (thin black lines). The cloud outline is delineated by the gray shaded contour in (a) and (c) and by a thick black line in (b) and (d), which shows reflectivity echoes ≥ 5 dBZ. The 0ºC, -10ºC and -20ºC isotherms are also shown by the thin dashed black lines. (b) as in (a) but for the simulated electric field magnitude starting at 25 kV m^{-1} by increment of 25 kV m^{-1} (gray shading). Note that the due to terrain in northwest OK (location of this cross section), the lowest height level above sea level is set at *z*=0.75 km. (c) Non-inductive (color shading) and inductive (thick black line) charging rate (in pC m^{-3} s^{-1}) and (d) total space charge (in pC m^{-3}, color shading). Legends for the colors and shadings in (c) and (d) are shown at the bottom. Inductive charging rate contour intervals are the same as non-inductive charging. Note that the electric field magnitude in (b) and the space charge in (d) are shown after discharge. Figure adapted from Fierro et al. (2013).

More recently, cloud-scale (500-m) benchmark simulations for Hurricane Isaac (2012) have been successfully conducted with WRF-ARW on XSEDE resources using the recently implemented and optimized three-dimensional M01 discharge scheme, which in contrast to the former (ZM94) approach does constraint the discharge within a cloud volume characterized by potential exceeding the breakdown threshold and, hence, is able to differentiate between flash polarity.

This optimized code was adapted to run for hurricanes (e.g., inclusion of CCN prediction, Mansell and Ziegler 2013) and showed a performance at 500-m near real time with hourly eyewall (storm-total) FOD rate generally below 1000 (2000) after the first hour of electrification spin up (Fig. 3b).

In addition to the simulated flash origin densities (Fig. 3b), the M01 scheme also allows the computation of additional relevant lightning metrics such as flash extent densities (Fig. 3c) and number of source densities (Fig. 3d). At this particular time (1500UTC 28 Aug), the simulated eyewall exhibits a prominent wavenumber 1 asymmetry with the bulk of the convection located on the south/southeastern semicircle (or rear quadrants, Fig. 3a) with the observations showing, rather, stronger convection to in the left front quadrant (now shown). In contrast to the simulated intensity showing an average minimum surface pressure error of -6 hPa with respect to the best track data (Fig. 3b), the position and the track of the simulated storm showed overall remarkable agreement with the observations (not shown).

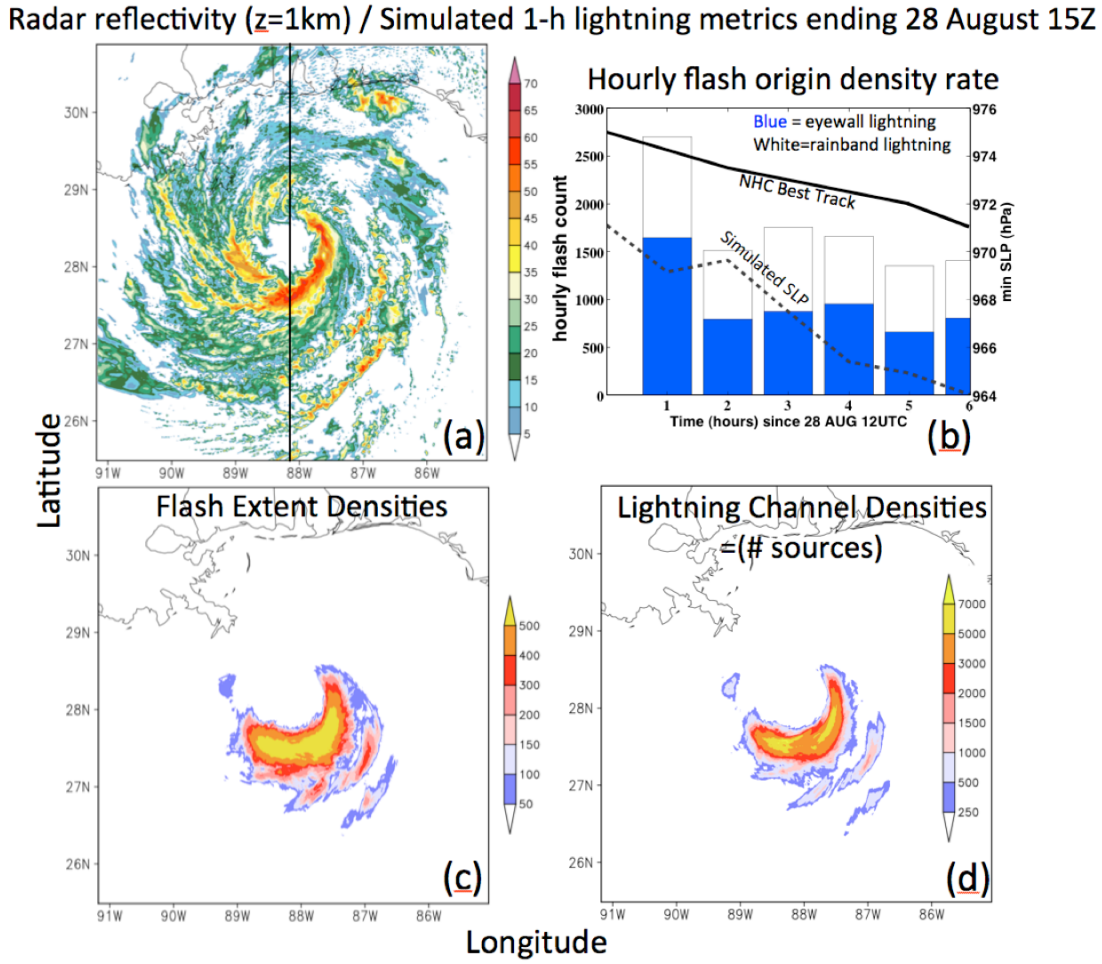

Figure 3. Simulated (a) z=1-km radar reflectivity and (b) time series of hourly flash origin densities (per 500-m x 500-m grid area) overlaid with observed (solid) and simulated (dashed) minimum sea level pressure (SLP, hPa). With the same units as (b), (c) shows the corresponding hourly flash extent densities and, finally, (d) the lightning source/channel densities. Hourly rates in (c) and (d) end at he time of the figure (28 Aug 1500UTC). The black horizontal line in (a) denotes the location of the vertical cross section shown in the remaining figures. In the M01 scheme, a lightning channel is referred to a grid cell volume (i.e., dx x dy x dz) where a discharge occurs.

Vertical cross sections through the eyewall and the active convection to the south of the eyewall reveal very localized pockets of active non inductive (NI) and inductive charging, which are primarily confined within the mixed phase region between 5 and 9 km AGL (i.e., 0° to -20°C isotherms, Fig. 4a). Positive NI charging is primarily found below ~ 7km AGL (~-10°C isotherm) whilst negative NI occurs mainly above that level (Fig. 4a). Weak and generally negative inductive charging is found above -10°C and, overall, is about order of magnitude smaller than NI charging. Consistent with this vertical incloud charging arrangement, the 5-7km (7-10km) layer exhibits a larger number of negative (positive) lightning channel segments (Fig. 4b, c). Note that overall, the number of positive channel is greater by about a factor two, which would be consistent with a larger volume of net negative charge in that layer (i.e., 7-10 km).

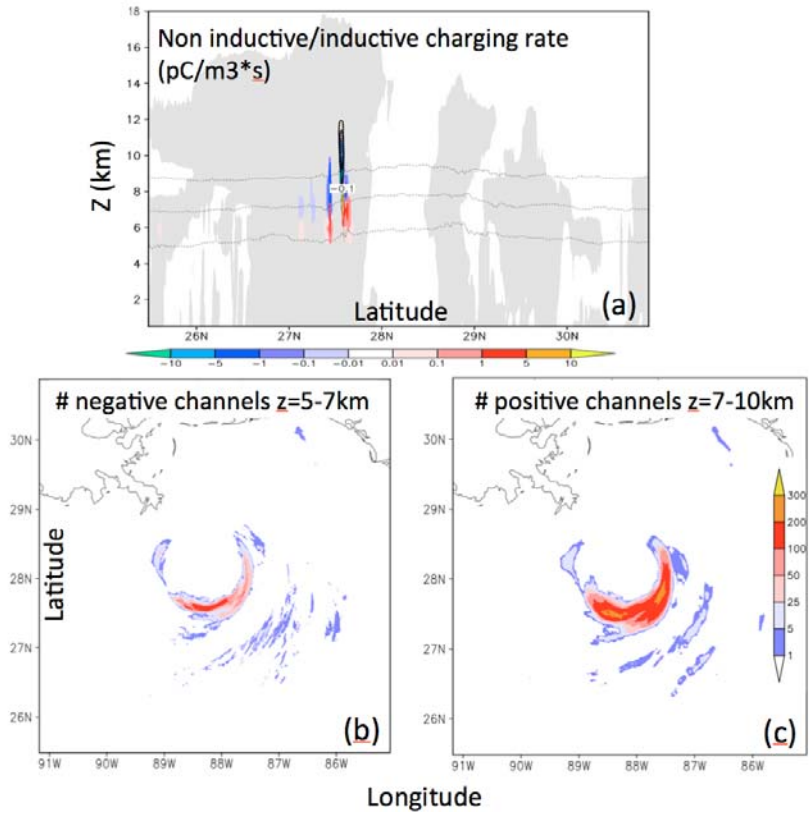

Figure 4. Non inductive (color shaded) and inductive (black contours) charging rates (pC m^{-3} s^{-1}) across the eyewall at 1500UTC 28 Aug with legends for colors shown at the bottom of (a). The contour levels for the inductive charging rates are the same as non-inductive charging rates. (b) and (c) shows horizontal cross sections as in Fig. 3 but for the number of negative (positive) channels integrated within the 5-7km (7-10 km) layer.

To illustrate the complexity of the lightning behavior in the eyewall convection, a vertical cross section of total positive and negative lightning channels in Fig. 5a and total net space charge through the eyewall in Fig. 5d show a dominant presence of net negative charge (and hence, positive, channels) within the 7-10 km layer. Above 10 km, the central dense overcast anvil cloud is largely composed of positive charge (Fig. 5d) on snow and ice crystals (no shown). Those positive charges aloft arise from the non-inductive graupel-ice collisions in the layer below it (7-10 km), which leaves the heavier

graupel with a net negative charge (Figs. 4a and 5d) while the opposite (positive) polarity of charge separated on the lighter ice crystals is lofted within the anvil. The large volume of net positive charge in the anvil explains the large number of negative channels above 10 km (Fig. 5a). Fig. 5a also indicates that most of the channels reaching altitudes below 1 km in the eyewall are negative, which would be consistent with the dominance of –CG flashes there.

In contrast to Rita, the areas of noteworthy (i.e., >100 pC m^{-3}) net charge across the hurricane are more discrete but still indicate a tendency towards a gross normal tripole charge structure (Fig. 5d), which can also be deduced from the vertical arrangement of the simulated lightning channels (Fig. 5a). This is largely a consequence of the ability of a 500-m grid to better resolve the typical characteristic length-scale of tropical updrafts (~0.5 to 1-km) in contrast to the 3-km simulation of Rita presented in Fierro et al. (2013), which clearly overestimated the updraft (and thus charge) volume in the eyewall.

The largest electric field magnitudes (40+ kV m^{-1}, after discharge) are collocated in between regions of opposite polarity of net space charge generally exceeding 50 pC m^{-3} (Fig. 5c, d). The presence of moderate electric fields (~20-40 kV m^{-1}) above the central dense overcast arises from this lightning model currently not including explicit treatment of small ions (drift and attachment), which would otherwise yield to the development of a screening layer at the cloud boundary (and reduce the fields above the anvils). Although this model includes a simplistic screening layer parameterization (Ziegler et al., 1991, which was not activated in this benchmark simulation.

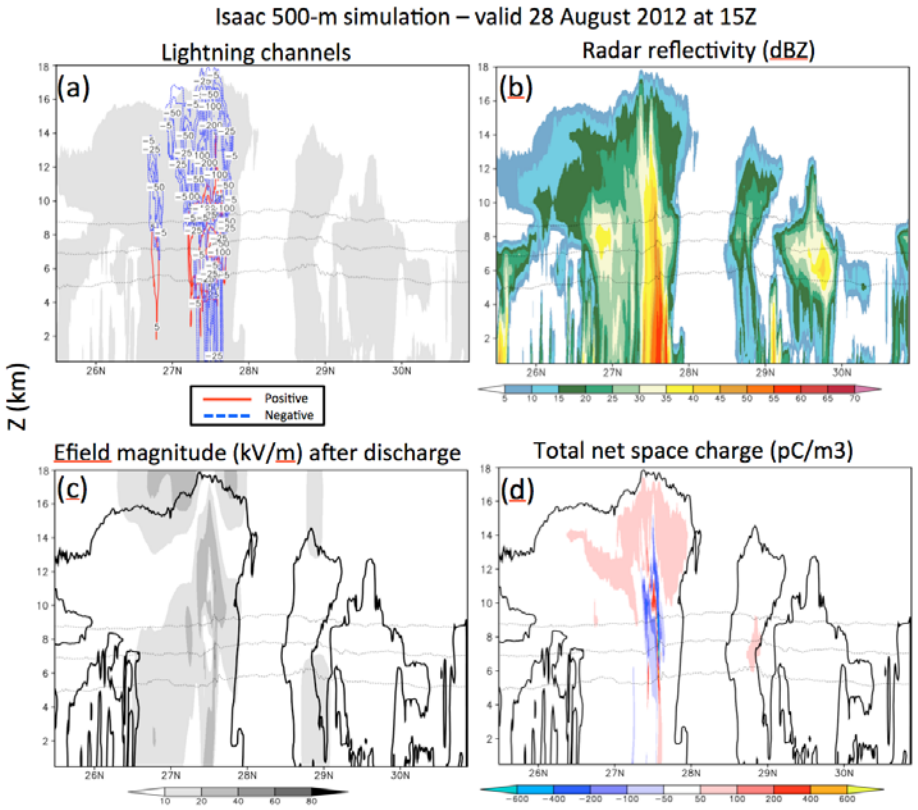

Figure 5. Simulated (a) positive (red) and negative (blue line) 1-h accumulated lightning channels, (b) radar reflectivity (in dBZ), (c) electric field magnitude in kV m^{-1} and (d) positive (red) and negative (blue line) total space charge (in pC m^{-3}) across the eyewall of Isaac at 1500 UTC August 28 2012 using the 3D M01 discharge scheme.

By virtue of being three dimensional and resolving the discharge process of individual flash instead of considering the discharge process as a bulk collective process across the entire simulation domain (ZM94), the M01 scheme is more computationally expensive than ZM94 for the same flash rates. Ongoing work has been focusing on optimizing the M01 scheme for real hurricane case studies with a targeted horizontal grid spacing of O(250m).

CONCLUSIONS

A computationally efficient electrification model with explicit charging and discharge physics has been implemented within the WRF-ARW numerical prediction model. The efficiency and performance of a recently implemented three dimensional discharge parameterizations were tested through convection-resolving (*dx*=500-m) model simulations of a tropical cyclone. Overall, the simulated spatial flash pattern exhibited reasonable agreement with available observations for this and other hurricanes (e.g., Cecil et al. 2002).

Modeling work in this relatively unexplored research area (i.e., tropical cyclone electrification) is desirable to understand for instance the physical linkages between lightning activity and intensity changes of a TC, behavior reported and well-recognized by several investigators (e.g., Molinari et al. 1999; DeMaria et al. 2012, Fierro et al. 2011). Most importantly, given the upcoming first launch of the Geostationary Operational Environmental Satellite "R" series (GOES-R, Gurka et al. 2006; Goodman et al. 2012, 2013) in 2015, this research is warranted and critical towards developing the next generation lightning predictors for routine assimilation of lightning information within NWP models or statistical prediction models (e.g., SHIPS, Kaplan et al. 2010). This capability becomes even more attractive considering that lightning data does not suffer from paucity over mountainous and oceanic area in contrast to conventionally assimilated radar data.

ACKNOWLEDGMENTS

Funding was provided by NOAA/ Office of Oceanic and Atmospheric Research under NOAA-University of Oklahoma Cooperative Agreement NA11OAR4320072, U.S. Department of Commerce. This work was also supported by the NESDIS program, which is under the auspices of the National Oceanic and Atmospheric Administration of the U.S. Department of Commerce under Grant NOAA-NESDIS-OAR- NA08OAR4320904. Computer resources were provided by the Extreme Science and Discover Environment (XSEDE) and the Oklahoma Supercomputing Center for Education and Research (OSCER) hosted at the University of Oklahoma. The authors thank Scott Dembek for providing the 40-km NAM data and Ami Arthur for providing the NSSL three-dimensional NMQ radar mosaic data. Thanks also go out to Bill Callahan, Benny Chukrun, Stan Heckman, and Jim Anderson from Earth Networks for providing the total lightning data for two of the case studies.

REFERENCES

Brooks, I. M., C. P. R. Saunders, R. P. Mitzeva, and S. L. Peck 1997: The effect on thunderstorm charging of the rate of rime accretion by graupel, *Atmos. Res*., **43**, 277–295.

Cecil, D. J., E. J. Zipser, and S. W. Nesbitt, 2002: Reflectivity, ice scattering, and lightning characteristics of hurricane eyewalls and rainbands. Part I: Quantitative description. *Mon. Wea. Rev*., **130**, 769–784.

DeMaria, M., R.T. DeMaria, J.A. Knaff, and D.A. Molenar, 2012: Tropical cyclone lightning and rapid intensity change. *Mon. Wea. Rev*., **140**, 1828-1842.

Dendy, J. E. Jr. 1987: Two Multigrid methods for three-dimensional problems with discontinuous and anisotropic coefficients, SIAM, *J. of Scientific and Statistical Computing*, **Vol. 8**.

Dendy J. E. and J. D. Moulton, 2010: Black Box Multigrid with coarsening by a factor of three. *Numer. Linear Algebra Appl*., **17**, 577–598. doi: 10.1002/nla.705

Emersic, C. and C.P.R. Saunders, 2010: Further laboratory investigations into the relative diffusional growth rate theory of thunderstorm electrification. *Atmos. Res*., **98**, 327-340.

Fierro, A. O., M. S. Gilmore, E. R. Mansell, L. J. Wicker and J. M. Straka, 2006: Electrification and lightning in an idealized boundary-crossing supercell simulation of 2 June 1995. *Mon. Wea. Rev.*, **134**, 3149–3172.

Fierro, A. O., L. M. Leslie, E. R. Mansell, J. M. Straka, D. R. MacGorman and C. Ziegler, 2007: A high resolution simulation of the microphysics and electrification in an idealized hurricane-like vortex. *Meteor. and Atmos. Phys.*, Springer, DOI 10.1007/s00703-006-0237-0.

Fierro, A. O., L. M. Leslie, E. R. Mansell and J. M. Straka, 2008: Numerical simulations of the electrification and microphysics of the weakly electrified 9th February 1993 TOGA COARE squall line: Comparisons with observations. *Mon. Wea. Rev*, **136**, 364-379.

Fierro, A. O and J. M. Reisner, 2011: High-resolution simulation of the electrification and lightning of hurricane Rita during the period of rapid intensification. *J. Atmos. Sci*, **68**, 477-494.

Fierro, A. O, X-M. Shao, J. M. Reisner, J. D. Harlin and T. Hamlin, 2011: Evolution of eyewall convective events as indicated by intra-cloud and cloud-to-ground lightning activity during the rapid intensification of Hurricanes Rita and Katrina. *Mon. Wea. Rev.*, **139**, 1492-1504.

Goodman S. J., R. J. Blakeslee, W. J. Koshak, D. Mach, J. Bailey, D. Buechler, L. Carey, C. Schultz, M. Bateman and E. McCaul, 2013: The GOES-R Geostationary Lightning Mapper (GLM). *Atmos. Res*., 125-126, 34-49.

Goodman, Steven J., and Coauthors, 2012: The GOES-R Proving Ground: Accelerating User Readiness for the Next-Generation Geostationary Environmental Satellite System. *Bull. Amer. Meteor. Soc.*, **93**, 1029–1040.

Gurevich, A. V., G. M. Milikh, and R. Roussel-Dupre, 1992: Runaway electron mechanism of air breakdown and preconditioning during a thunderstorm. *Phys. Lett. A*, **165**, 463–468.

Gurka, J. J., T. A. Schmit, T. M. Renkevens, M. M. Gunshor, and J. Li, 2006: 2006 update on baseline instruments for GOES-R series. Atmospheric and Environmental Remote Sensing Data Processing and Utilization II: Perspective on Calibration/ Validation Initiatives and Strategies, A. H. L. Huang and H. J. Bloom, Eds., International Society for Optical Engineering (SPIE Proceedings, Vol. 6301), 63010H, doi:10.1117/12.683701.

Helsdon, J. H., Jr., and R. D. Farley, 1987: A numerical modeling study of a Montana thunderstorm, 2, Model results versus observations involving electrical aspects, *J. Geophys. Res*., **92**, 5661–5675.

Helsdon, J. H., Jr., W. A. Wojcik, and R. D. Farley 2001: An examination of thunderstorm-charging mechanisms using a two-dimensional storm electrification model, *J. Geophys. Res*., **106**, 1165–1192.

Kaplan, J., M. DeMaria, and J.A. Knaff, 2010: A revised tropical cyclone rapid intensification index for the Atlantic and eastern North Pacific basins. *Wea. Forecasting*, **25**, 220-241.

MacGorman, D. R., J. M. Straka and C. L. Ziegler, 2001: A lightning parameterization for numerical cloud models. *J. Appl. Meteor*., **40**, 459–478.

Mansell, E. R., D. R. MacGorman, C. L. Ziegler and J. M. Straka, 2002: Simulated three-dimensional branched lightning in a numerical thunderstorm model. *J. Geophys. Res*., **107**, 4075, doi:10.1029/2000JD000244.

Mansell, E. R., D. R. MacGorman, C. L. Ziegler and J. M. Straka, 2005: Charge structure and lightning sensitivity in a simulated multicell thunderstorm. *J. Geophys. Res*., **110**, D12101, doi:10.1029/2004JD005287.

Mansell, E. R., C. L. Ziegler, 2013: Aerosol Effects on Simulated Storm Electrification and Precipitation in a Two-Moment Bulk Microphysics Model. *J. Atmos. Sci.*, **70**, 2032–2050.

McCaul, E. W., S. J. Goodman, K. M. LaCasse, and D. J. Cecil, 2009: Forecasting lightning threat using cloud-resolving model simulations. *Wea. Forecasting*, **24**, 709–729.

Molinari, J., P. Moore, and V. Idone, 1999: Convective structure of hurricanes as revealed by lightning locations. *Mon. Wea. Rev*., **127**, 520–534.

Rawlins, F. 1982: A numerical study of thunderstorm electrification using a three dimensional model incorporating the ice phase. *Q. J. Roy. Meteor. Soc*., **108**, 779–800.

Saunders, C. P. R., and S. L. Peck, 1998: Laboratory studies of the influence of the rime accretion rate on charge transfer during crystal/graupel collisions. *J. Geophys. Res.*, **103** (D12), 13949–13956.

Shao, X. M, M. Stanley, A. Regan, J. Harlin, M. Pongratz, and M. Stock, 2006: Total lightning observations with the new and improved Los Alamos Sferic Array (LASA). *J. Atmos. Oceanic Tech- nol*., **23**, 1273–1288.

Stolzenburg, M., W. D. Rust, B. F. Stull, and T. C. Marshall, 1998: Electrical structure in thunderstorm convective regions. 1. Mesoscale convective systems. *J. Geophys. Res.*, **103,** 14059–14078.

Takahashi, T., 1978: Riming electrification as a charge generation mechanism in thunderstorms. *J. Atmos. Sci.*,

35, 1536–1548.

Takahashi, T., 1984: Thunderstorm electrification—A numerical study. *J. Atmos. Sci.*, **41**, 2541–2558.

Takahashi, T., and K. Miyawaki, 2002: Reexamination of riming electrification in a wind tunnel, *J. Atmos. Sci*., **59**, 1018–1025

Wiens, K. C., S. A. Rutledge, and S. A. Tessendorf, 2005: The 29 June 2000 supercell observed during STEPS. Part II: lightning and charge structure. *J. Atmos. Sci*., **62**, 4151–4177.

Williams, E. R., 1989: The tripole structure of thunderstorms. *J. Geophys. Res*., **94**: 13151- 13167.

Ziegler, C. L., D. R. MacGorman, J. E. Dye, and P. S. Ray, 1991: A model evaluation of non-inductive graupel-ice charging in the early electrification of a mountain thunderstorm. *J. Geo- phys. Res.*, **96**, 12 833–12 855.

Ziegler, C. L. and D. R. MacGorman, 1994: Observed lightning morphology relative to modeled space charge and electric field distributions in a tornadic storm. *J. Atmos. Sci.*, **51**, 833–851.